



PHASE-CORRELATION AND SPARSE MODELLING FOR DAMAGE DETECTION DUE TO THE 2018 SULAWESI-EARTHQUAKE TSUNAMI

L. Moya^(1,2), E. Mas⁽³⁾, and S. Koshimura⁽⁴⁾

⁽¹⁾ Researcher, IRIDeS, Tohoku University, Japan, lmoyah@irides.tohoku.ac.jp

⁽²⁾ Principal Investigator, CISMID, National University of Engineering, Peru, lmoyah@uni.pe

⁽³⁾ Associate Professor, IRIDeS, Tohoku University, Japan, mas@irides.tohoku.ac.jp

⁽⁴⁾ Professor, IRIDeS, Tohoku University, Japan, koshimura@irides.tohoku.ac.jp

Abstract

On September 28, 2018, a magnitude Mw 7.5 earthquake occurred at 75 km north from the city of Palu, Central Sulawesi, Indonesia. The earthquake induced catastrophic effects, such as a series of tsunamis, landslides, and liquefaction. It has been reported more than 70,000 damaged houses. In this event, significant permanent ground deformation was observed. In fact, the ruptured fault crosses the city of Palu. In this kind of disaster events, one of the earliest needs is the identification of collapsed buildings, which may contain survivors trapped inside. An automatic procedure for such purpose can be performed from a pair of satellite images taken before and after the event. The fundamental basis lies in the detection of changes between both images. However, before detecting changes, the pair of images must be perfectly aligned. In ordinary situations, aligning a pair of images, a pre-process termed image co-registration, is a straightforward procedure. In general lines, first, some ground control points are identified, manually or automatically, in both images and, second, use them for mapping one image by some linear or polynomial transformation. Unfortunately, because image co-registration assumes smooth transformation, it did not work well for the case of the 2018 Sulawesi earthquake-tsunami. The complex ground deformations due to the fault line and the liquefaction could not be removed by linear/polynomial transformation. In this paper we report a novel procedure to identify the areas affected by the earthquake and tsunami. The method does not require image co-registration. It is based on the application of *phase-correlation* and *sparse modeling*. Consider the phase-correlation a function whose input is the two images and its output is a bi-dimensional array. On ideal conditions, phase-correlation exhibit a distinctive peak in areas without damage (no-change); otherwise, there is no such peak. In real scenarios, though, such a trend is difficult to identify in medium/low-resolution images. Therefore, statistical learning with sparsity, more precisely sparse logistic regression based on ℓ_1 -regularization, is employed here to identify the significant components of the phase-correlation for the identification of collapsed buildings. The proposed framework was applied to optical and microwave images and the results achieved high accuracy.

Keywords: The 2018 Sulawesi earthquake-tsunami, phase-correlation, sparse modeling, damage mapping



1. Introduction

The identification of damage to the urban area in the aftermath of a large-scale disaster is an important task in emergency response and recovery activities [1-8]. Satellite remote sensing, because its wide coverage, is probably the only way to inspect the completely affected area produced by a large disaster. The most efficient method to identify damage is the comparison of a pair of images recorded before (*pre-event*) and after (*post-event*) the disaster in mention, an approach usually referred to as *change detection*. However, proper change detection analysis requires the two images to be perfectly aligned. Thus, a pre-process called *image registration* is always applied to the images in order to align one image with respect to the other.

Most of the image registration algorithms have a step in common, namely, the search for common points in both the pre-event and the post-event images. Such points are referred to as *ground control points* (GCPs). There is a trade-off between the number of GCPs and the precision of the image registration. A larger number of GCPs require intense computation resources, whereas a low number of GCPs can compromise the precision of the image registration. Once the GCPs are selected, the offsets in each GCP are measured; then, one image is resampled to be aligned with the other. Common resampling techniques are *similarity warping* and *polynomial warping* [9]. It has been observed recently that standard image registration techniques cannot correct complex ground deformation induced by earthquakes of large magnitudes. Coseismic deformation near the fault line, liquefaction, and landslides are such examples.

In this study, we identify the collapsed buildings due to the 2018 Mw 7.5 Sulawesi Indonesia earthquake-tsunami, where complex ground deformations were observed. Instead of using a significantly large amount of GCPs to reduce the effect of the complex deformations, we propose to eliminate the image registration processing from the processing chain for damage mapping. Hence, we introduce the use of *phase correlation* and the ℓ_1 -regularized logistic regression classifier as a new alternative. The phase correlation is a bi-dimensional signal computed from a pair of images that shows a property that is independent of the offset between the images. However, previous studies have shown that only a few components of the phase correlation signal contain information regarding the degree of similarity between the pair of images. Thus, an efficient change detection model must be able to identify the relevant components of the phase correlation. We use the ℓ_1 -regularized logistic regression classifier for this purpose because it produces a sparse model for classification [10].

2. Fundamental basis

2.1 The phase correlation

Consider that the bi-dimensional discrete functions $f(n_1, n_2)$ and $g(n_1, n_2)$ represent the pre-event and post-event images respectively, and are defined as:

$$\begin{aligned} f(n_1, n_2) &= f(x, y)|_{x=n_1T_1, y=n_2T_2} \\ g(n_1, n_2) &= f(x - x_0T_1, y - y_0T_2)|_{x=n_1T_1, y=n_2T_2} \end{aligned} \quad (1)$$

where n_1 and n_2 denotes the discrete domains, T_1 and T_2 denotes the pixel resolution in the horizontal and vertical axis, and x_0T_1 and y_0T_1 denotes the offset between the images in the x and y axis. The normalized cross power spectrum is defined as:

$$R(u, v) = \frac{F(u, v)\overline{G(u, v)}}{|F(u, v)G(u, v)|} = e^{j(ux_0+vy_0)} \quad (2)$$

where $F(u, v)$ and $G(u, v)$ denotes the discrete Fourier transform of $f(n_1, n_2)$ and $g(n_1, n_2)$, respectively. The phase correlation is referred as the inverse discrete Fourier transform of R . The phase correlation has the following properties: (i) If f and g are identical images, then the phase correlation is a unit pulse with the peak centered; (ii) if g is identical to f but circular-shifted by integer values x_0 and y_0 , then the phase correlation is a unit pulse with a peak value located at a position (x_0, y_0) with respect of the center; (iii) if g



is identical to f but circular-shifted by non-integer values x_0 and y_0 , then the phase correlation no longer shows a unit pulse, but rather a peak whose shape consists of more than one component; (iv) if f and g are different images, then the phase correlation does not exhibit any peak.

In real practice, the evaluation of phase correlation is more subtle. Two images recorded in the same area but on different dates are not precisely identical. Although they exhibit a high degree of similarity, seasonal changes on vegetation or the presence of cars only in one image are examples of subtle differences between the referred images. Fig. 1a shows the visible bands of two images taken at an urban area that did not experience any damage. As can be observed, the images are not completely identical. The phase correlation computed for each pair of bands is depicted in Fig. 2a. Note that although the peak is observed, there is background noise in the signal. On the other hand, areas affected by an arbitrary large scale disaster will exhibit a high degree of dissimilarity; however, there is some degree of similarity represented by non-collapsed buildings. Fig. 1b shows a pair of images taken before (top) and after (bottom) a tsunami arrived. It is observed a great amount of debris and some of the buildings were washed away. Nevertheless, it is also observed that some buildings remain non-collapsed. The phase correlation computed for this case (Fig. 2b) does not exhibit a clear peak and the level of background noise is larger than that computed from the case of the non-damaged urban area (Fig. 2a).

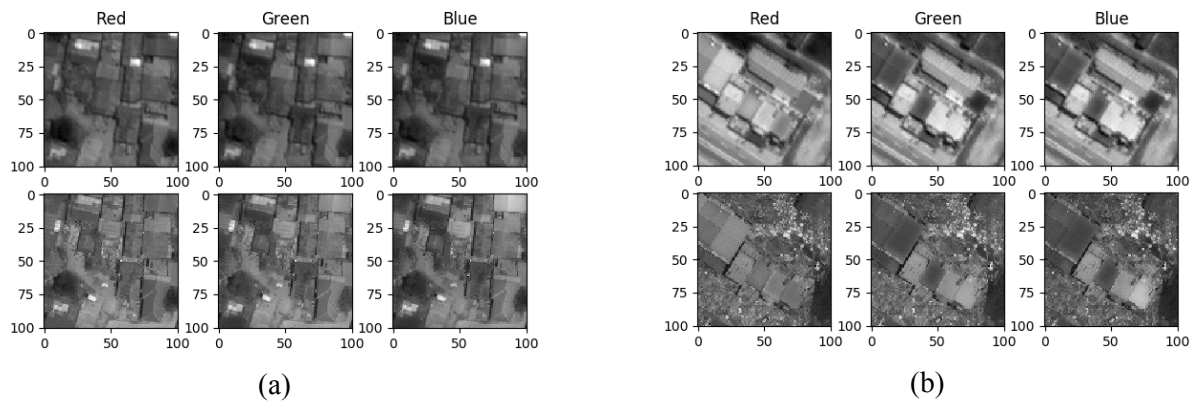


Fig. 1 – Examples of visible spectral bands taken at urban areas. (a) Non-damaged urban area. (b) Tsunami affected urban area.

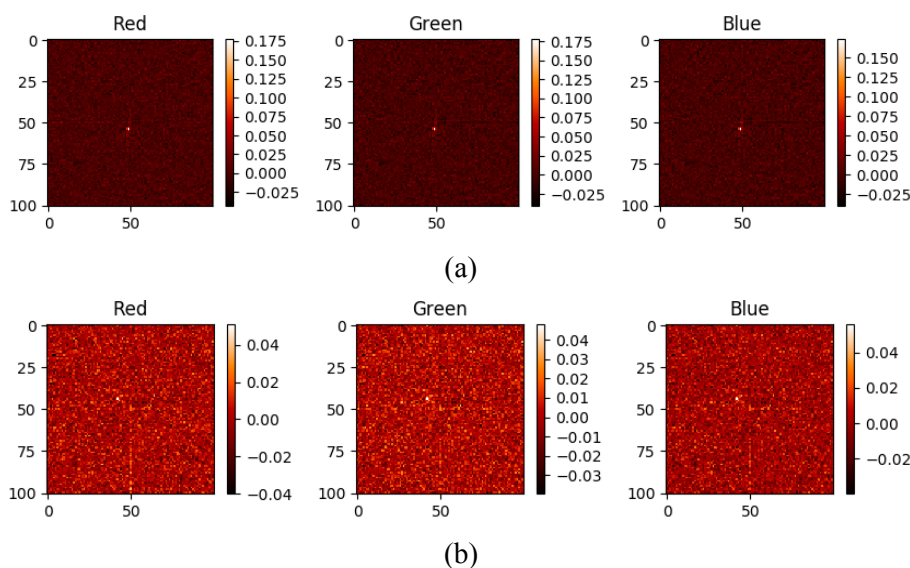


Fig. 2 – Phase correlation computed in urban areas. (a) The non-damaged urban area shown in Fig. 1a. (b) The tsunami affected urban area shown in Fig. 1b.



2.2 The ℓ_1 -regularized logistic regression classifier [10]

A classifier is a function that assigns a sample i certain label/class z_i by using as input a set of features arranged in a vector r_i . Here, we use a binary class $z_i \in \{-1, 1\}$, where the label -1 indicates that the sample represents a damaged area, and the label 1 indicates the sample represents a non-damaged area. As the name of the section suggests, we use the logistic regression function:

$$Pr(z_i = 1|r_i) = \frac{\exp(\beta_0 + \beta^T r_i)}{1 + \exp(\beta_0 + \beta^T r_i)} \quad (3)$$

where β^T is a vector of regression coefficients, β_0 is an intercept term, and $Pr(z_i = 1|r_i)$ denotes the probability that $z_i = 1$. If $Pr(z_i = 1|r_i) \geq 0.5$, then it is assumed $z_i = 1$; otherwise $z_i = -1$. In order to use Eq. (3), the parameters β_0 and β^T need to be tuned, a process often referred to as *model calibration*.

The model calibration is performed using a set of samples from which their class/label are known in advance. The model calibration is based on the following optimization problem:

$$\min_{\beta_0, \beta} \left\{ C \sum_{i=1}^N \log(1 + \exp(-z_i(\beta_0 + \beta^T r_i))) + \|\beta\|_1 \right\} \quad (4)$$

where $\|\cdot\|_1$ denotes the ℓ_1 -norm. The use of ℓ_1 -norm yields sparse solutions. A sparse solution refers to a solution in which the vector β has relatively few non-zero components. The parameter C is associated with the sparse level (i.e., the percentage of zero components of the vector β) of the solution. A low C -value will yield a high level of sparsity, whereas a large C -value produces a low level of sparsity.

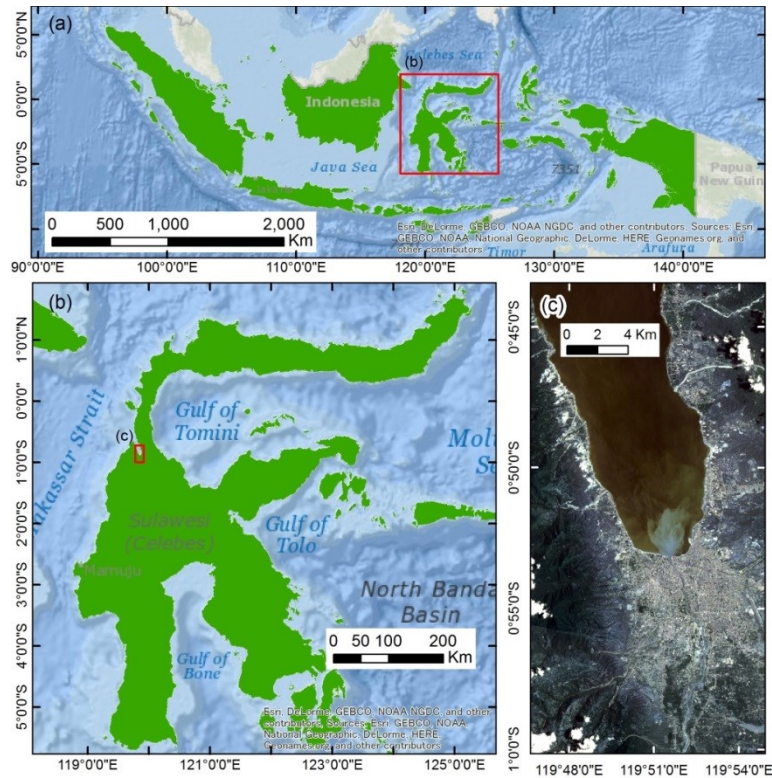


Fig. 3 – Location of the study area. (a) location of the Sulawesi island (red rectangle) within Indonesia (green polygons). (b) Location of the study area (red rectangle) within the Sulawesi island. (c) Planet image recorded after the 2018 Sulawesi Indonesia earthquake-tsunami in the study area.



Fig. 4 – complex ground deformation at the central coast of the city of Palu, Sulawesi. (a) Coseismic displacement (yellow arrows) around the Palu-Koro fault line (dashed red line). (b) Liquefaction.

3. The 2018 Sulawesi Indonesia earthquake-tsunami

On 28 September 2018, an earthquake of moment magnitude (M_w) of 7.5 occurred 75 km north of the city of Palu, Central Sulawesi, Indonesia. The earthquake is associated with an active strike-slip fault called Palu-Koro [11]. Important secondary effects of this earthquake are a tsunami, landslides, and liquefaction. Overall, as of 25 October 2018, this earthquake left approximately 68,451 damaged houses, 2081 casualties, and 4438 injured people [12]. The urban areas most affected were located in the city of Palu and its surroundings, but also it was the area that experienced the complex ground deformation. Fig. 4a depicts the coseismic displacement as yellow arrows near the central area of the coast of Palu city. The red dashed line shows the location of the fault line. It can be observed that each side of the fault line exhibit a different trend on the coseismic displacement. Fig. 4b shows a liquefaction area, another source of complex local ground deformation. Because the liquefaction area is significantly large, it is cataloged as a landslide for some studies. It has been recently pointed out that communal irrigation had a significant impact on this phenomenon [13].

3.1 Damaged mapping procedure in urban footprints

In order to prepare a large scale damage mapping due to the earthquake, visual and near-infrared (VNIR) spectral bands of 3-m resolution are used. Planet provided the images under an early disaster response framework [14]. Figure 3c shows the post-event image recorded on 2 October 2018. Also, a second image recorded in 18 September 2018 is used as a pre-event image. Note that both images are not co-registered. Damage identification is strictly applied to urban areas (Fig. 6a). Hence, the urban footprint was first mapped using eleven Sentinel-2 imagery recorded during 2018, but before the occurrence of the earthquake [15]. The resulted urban footprint map is a grid of $10 \times 10\text{-m}^2$ resolution. Then, for each grid-cell, the phase correlation is computed using the pre- and post-event Planet images. The phase correlation is computed using a Planet sub-images of 21×21 -pixels closest to the grid-cell. Recall that each image has four spectral bands (red, green, blue, and near-infrared), and thus, the phase correlation is computed four times.

The ℓ_1 -regularized logistic regression is used to classify whether a grid-cell is damaged or not. The feature vector r_i showed in Eq. (3) is constructed from the phase correlation in the following manner: First, the phase correlation is computed. As referred above, the sub-images of size 21×21 are used to compute the phase correlation; therefore, the phase correlation has the same size. Second, The location of the maximum value of the phase correlation is identified. Third, a sub-matrix of the phase correlation with size 11×11 , and with the maximum phase correlation value at the center, is used as a feature. Each phase correlation sub-matrix contributes with $11 \times 11 = 121$ features. Hence, a sample/grid-cell has 484 features (4 spectral bands), which are stored in the vector r_i .

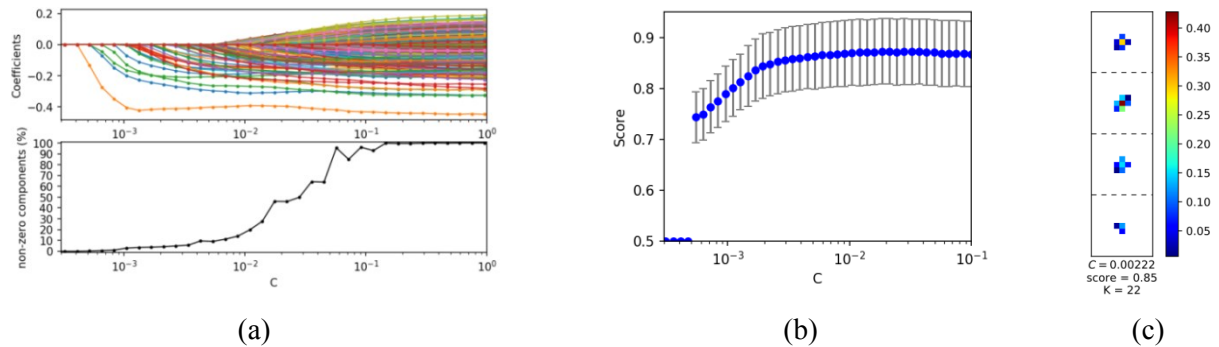


Fig. 5 – Sparsity analysis. (a) Relationship between the parameter C and the level of sparsity. (b) Relationship of the parameter C and the accuracy score of the predictions. (c) Coefficients of vector B arranged in a matrix format computed with $C=0.00222$.

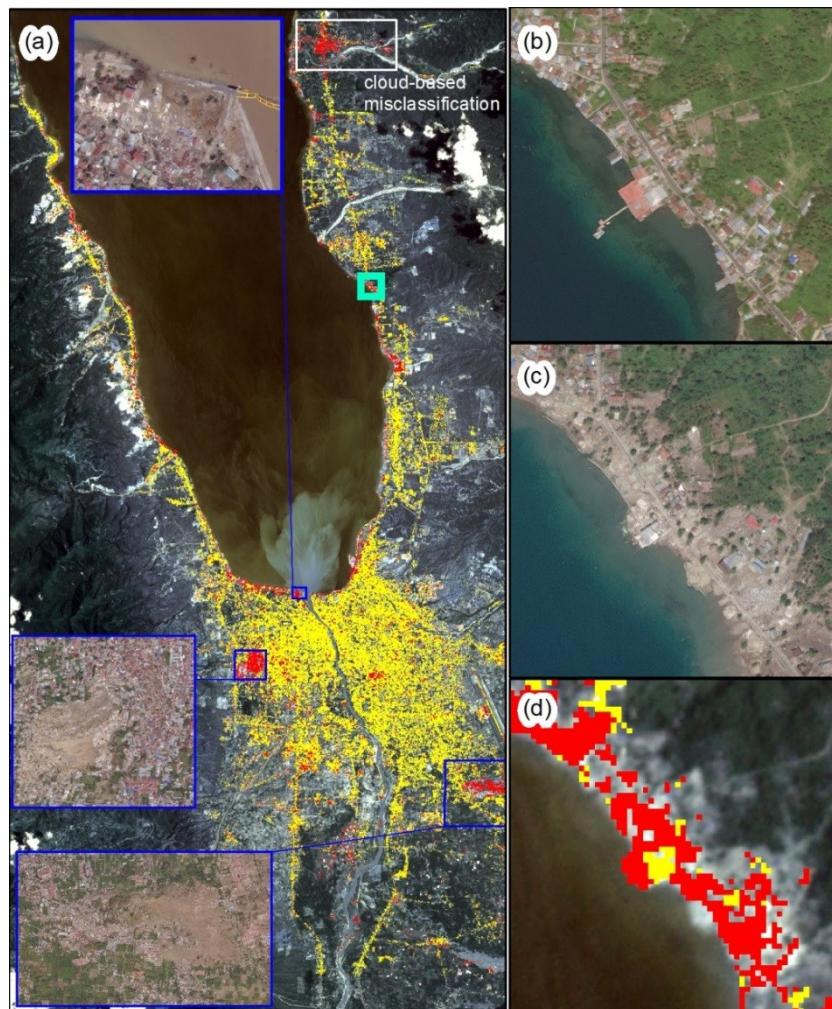


Fig. 6 – Predictions of damaged (red pixels) and non-damaged (yellow pixels) in urban footprint areas. (a) Complete study area. (b) Pre-event high-resolution image of a non-inspected area. (c) Post-event high-resolution image of the same area shown in (b). (d) Predicted damage using the proposed method on medium-resolution VNIR images.

The building damage inventory provided by the Copernicus Emergency Management Service [16] is employed in the model calibration process. The damage inventory was performed by visual inspection of optical imagery of 0.5-m resolution. Buildings classified as destroyed and non-damaged are used to classify



the grid-cells to damaged-based changed ($z_i = 1$) and non-changed ($z_i = -1$) areas, respectively. The model calibration is performed using Eq. (4) from a range of values for the C parameter. The relationship between every coefficient β_i and C is shown at the top of Fig. 5a, often referred to as *coefficients path* figure. Note that as C approaches to zero, most of the components of β_i equals zero. On the other hand, when C approaches to one, all the coefficients of β_i differ from zero. The relationship between the percentage of non-zero components of β and C is illustrated at the bottom of Fig. 5a. The performance of the classifier in terms of accuracy under a range of C -values is shown in Fig. 5b; where the percentage of correctly classified samples from the building damage inventory is used as a *score*. The 10-fold cross-validation is used to compute the score. Namely, the damage inventory is randomly divided into 10-subsets, from which nine subsets are used for model calibration (*training data*), and the remaining subset is used to compute the score (*testing data*). This process is repeated ten times, each using a different subset as testing data. From Fig. 5b, the blue points denote the averaged score and the bar denotes the limits of the averaged score plus/minus the standard deviation. Observe that for C values lower than or equal 0.0004, the score is 50%. Then, the accuracy increases at a high rate until about $C = 0.002$. For C -values greater than 0.002, the score remains almost unchanged. Thus, we use a $C = 0.002$ as the optimal value because it yields the lowest number of non-zero components of β with the highest accuracy. Fig. 5c shows the coefficients of β_i re-arranged as four matrices of 11×11 , which are associated with the phase correlation sub-matrices used to construct the feature vector r_i . Note that (i) only 22 components of β are non-zero, (ii) they include the components associated to the center of each submatrix (i.e., the maximum value of the phase correlation), and (iii) the other components are located closest to the location of the center of a submatrix.

3.2 Results

Once the ℓ_1 -regularized logistic regression was calibrated, it was applied to the study area shown in Fig. 3c. The changes between the pre-event and post-event Planet images are shown in Fig. 6a. The yellow pixels denote grid-cells where no changes are detected, whereas the red pixels denote grid-cells where changes are detected. Considering that the acquisition dates of the images differ only two weeks, we can assume that most of the observed changes are associated with the occurrence of the earthquake-tsunami. Fig. 6a shows closer looks of high-resolution optical images at specific areas that suffered tsunami and liquefaction damage. Our results, computed from medium resolution (3-m) images, are consistent with high-resolution (0.5-m) post-event images. However, because these areas were dramatically affected, it was included in the damage inventory that was used for model calibration. The true relevance of this semi-automatic damage mapping procedure is that it can search for much larger areas without human effort. For instance, Fig. 6b-d shows a tsunami-affected area that was not reported in the damage inventory but reported in our results. Fig. 6b and 6c show the pre-event and post-event high-resolution optical imagery. Fig. 6c shows the post-event Planet image of the same area, and at the top is shown our results. The location of fig. 6b-d is shown in fig. 6a as a cyan rectangle. It is worth to point out the limitations of the results as well. For instance, the white rectangle at the top of Fig. 6a shows a large area classified as changed; however, it was the result of the presence of clouds in the pre-event image rather than damage due to the earthquake-tsunami.

4. Conclusions

In this paper, we report a procedure to identify changes between a pair of images to identify the effects of a large scale disaster. The procedure does not require the images to be co-registered, a process that requires significant runtime and it is very challenging when complex local ground deformations exist in the area of interest. The method proposed the use of phase correlation as a feature signal because it exhibits a clear peak if the images are very similar; otherwise, no peak is observed. In order to identify the components of the phase correlation signal that makeup such a peak, the ℓ_1 -regularized logistic regression is employed. The proposed procedure was applied to a pair of visual and near-infrared spectral bands images with 3-m resolution. The images were acquired before and after the occurrence of the 2018 Sulawesi Indonesia earthquake-tsunami, with a time-baseline of about two weeks. Thus, most of the detected changes are associated with the earthquake-tsunami effects. Our results show an agreement of 85% with a building



damage inventory. Therefore, the results indicate that it is possible to identify changes between images that are not co-registered. Furthermore, we showed that the proposed method could be used to complement damage inventory based on human visual inspection.

5. Acknowledgements

This study was partly funded by the J-Rapid project number JPMJRR1803; The JST CREST project number JP-MJCR1411; the JSPS Kakenhi Program project number 17H06108; and the National Fund for Scientific, Technological and Technological Innovation Development (Fondecyt – Peru) within the framework of the “Project for the Improvement and Extension of the Services of the National System of Science, Technology and Technological Innovation” (contract number 038-2019).

6. References

- [1] Yamazaki F, Matsuoka M (2007): Remote sensing technologies in post-disaster damage assessment. *Journal of Earthquake and Tsunami*, 1 (3), 193-210.
- [2] Matsuoka M, Nojima N (2010): Building damage estimation by integration of seismic intensity information and I-ban sar imagery. *Remote Sensing*, 2 (9), 2011-2126.
- [3] Matsuoka M, Yamazaki F (2004): Use of satellite SAR intensity imagery for detecting building areas damaged due to earthquakes. *Earthquake Spectra*, 20 (3), 975-994.
- [4] Moya L, Yamazaki F, Liu W, Chiba T (2017): Calculation of coseismic displacement from lidar data in the 2016 Kumamoto, Japan, earthquake. *Natural Hazards and Earth System Sciences*, 17 (1), 143-156.
- [5] Moya L, Mas E, Adriano B, Koshimura S, Yamazaki F, Liu W (2018): An Integrated method to extract collapsed buildings from satellite imagery, hazard distribution and fragility curves. *International Journal of Disaster Risk Reduction*, 31, 1374-1384.
- [6] Moya L, Marval Perez LR, Mas E, Adriano B, Koshimura S, Yamazaki F (2018): Novel unsupervised classification of collapsed buildings using satellite imagery, hazard scenarios and fragility functions. *Remote Sensing*, 10 (296), 16 pages.
- [7] Moya L, Zakeri H, Yamazaki F, Liu W, Mas E, Koshimura S (2019): 3D gray level co-occurrence matrix and its application to identifying collapsed buildings. *ISPRS Journal of Photogrammetry and Remote Sensing*, 149, 14-28.
- [8] Moya L, Endo Y, Okada G, Koshimura S, Mas E (2019): Drawback in the change detection approach: False detection during the 2018 western Japan floods. *Remote Sensing*, 10 (296), 19 pages.
- [9] Canty M (2014): *Image analysis, classification and change detection in remote sensing: with algorithms for ENVI/IDL and python*, Taylor & Francis, 3rd edition.
- [10] Hastie T, Tibshirani R, Wainwright M (2015): *Statistical learning with sparsity: The lasso and generalizations*. Chapman & Hall/ CRC Press. 1st edition.
- [11] Socquet A, Hollingsworth J, Pathier E, Bouchon M (2019): Evidence of supershear during the 2018 magnitude 7.5 Palu earthquake from space geodesy. *Nature Geoscience*, 12, 192-199.
- [12] The AHA Centre (2018): Situation update No. 15-Final; M 7.4 Earthquake & Tsunami Sulawesi, Indonesia. Available at: <https://ahacentre.org/situation-update/situation-update-no-15-sulawesi-earthquake-26-october-2018/>
- [13] Watkinson IM, Hall R (2019): Impact of communal irrigation on the 2018 Palu earthquake-triggered landslides. *Nature Geoscience*, 12, 940-945.
- [14] Planet (2018): Earthquake and tsunami in Indonesia. Available at: <https://www.planet.com/disaster/earthquake-indonesia-2018-09-28/>
- [15] Copernicus (2018): Copernicus Open Access Hub. Available at: <https://scihub.copernicus.eu/>
- [16] Copernicus Emergency Management Service (2018): EMSR317: Earthquake in Indonesia. Available at: <https://emergency.copernicus.eu/mapping/list-of-components/EMSR317>